IEEE Access
Multidisciplinary | Rapid Review | Open Access Journal

Received December 13, 2019, accepted February 17, 2020, date of publication February 27, 2020, date of current version March 12, 2020.

Digital Object Identifier 10.1109/ACCESS.2020.2976557

Optical Coherence Tomography/Angiography-Guided Tumor Ablation With a Continuous-Wave Laser Diode

MENG-TSAN TSAI[1,2], WEN-JU CHEN[1], TING-YEN TSAI[3], HSIANG-CHIEH LEE[3,4], CHUN-CHIEH WANG[5,6], AND YA-JU LEE[7]

[1]Department of Electrical Engineering, Chang Gung University, Taoyuan 33302, Taiwan
[2]Department of Neurosurgery, Chang Gung Memorial Hospital at Linkou, Taoyuan 33306, Taiwan
[3]Graduate Institute of Photonics and Optoelectronics, National Taiwan University, Taipei 10617, Taiwan
[4]Department of Electrical Engineering, National Taiwan University, Taipei 10617, Taiwan
[5]Department of Medical Imaging and Radiological Sciences, Chang Gung University, Taoyuan 33302, Taiwan
[6]Department of Radiation Oncology, Chang Gung Memorial Hospital at Linkou, Taoyuan 33306, Taiwan
[7]Institute of Electro-Optical Science and Technology, National Taiwan Normal University, Taipei 11677, Taiwan

Corresponding authors: Hsiang-Chieh Lee (hclee2@ntu.edu.tw), Chun-Chieh Wang (jjwangucla@gmail.com), and Ya-Ju Lee (yajulee@ntnu.edu.tw)

This work was supported in part by the Chang Gung Memorial Hospital, Taiwan, under Grant CMRPD2H0242, and in part by the Ministry of Science and Technology of the Republic of China (ROC), Taiwan, under Grant MOST 105-2221-E-182-016-MY3, Grant 107-2627-M-007-005, Grant 108-2636-E-002-009, and Grant 107-2628-E-182-001-MY3.

ABSTRACT Laser ablation can be an effective modality for treatment, but it is complicated to apply continuous-wave (CW) light sources for laser ablation because of the unpredictable photothermal damage. In this study, an integrated theranostic system combining a low-cost CW laser diode with optical coherence tomography (OCT)/angiography (OCTA) was utilized for the *in vivo* ablation of tumor tissues. To examine the effect of laser exposure on tissue scattering characteristics, the OCT backscattering intensities of non-ablated and ablated tissues were analyzed, and the effect on the skin microvasculature produced by laser ablation was quantitatively evaluated. Moreover, the integrated system and the proposed method were implemented for the treatment of skin tumor on the mouse model. The obtained results indicate that the developed laser ablation system can effectively remove tumor tissues with controllable photodamage under OCT/OCTA guidance and that the system cost may be significantly reduced by using the CW laser diode.

INDEX TERMS Laser diode, laser ablation, biomedical optical imaging, angiography, medical diagnostic imaging, biophotonics.

I. INTRODUCTION

Laser therapy has become an alternative treatment solution in addition to conventional surgical resection by using high-intensity light to shrink or damage tissue [1], [2]. Its effects are produced via two main mechanisms corresponding to thermotherapy and photocoagulation [3], [4]. During thermotherapy, the optical energy of laser light is absorbed by the tissue leading to the thermal effect and tissue evaporation. When a high-intensity or high-power laser is applied, the irradiated cells can be severely damaged, changing the tissue composition. In contrast, photocoagulation is mainly caused by the absorption of red blood cells, leading to their coagulation and the formation of thrombi. The latter process results in ischemia, low oxygen levels, and poor nutrition transportation that are essential for tissue growth. Currently, photocoagulation has been commonly applied in ophthalmology and for the treatment of liver cancer [5], [6]. In the past, various lasers such as CO_2 and Nd:YAG ones were utilized for medical treatment [7], [8]. It was also demonstrated that either continuous-wave (CW) or pulsed-mode lasers could be used for laser therapy [9], [10]. In clinical applications, short-pulse lasers represent the most commonly used therapeutic tool because they are able to damage the irradiated tissues without melting the surrounding before heat accumulation occurs [11]. However, such short-pulse lasers are very expensive and bulky, which makes their clinical application extremely challenging.

Tumors (also known as neoplasms) are abnormal masses caused by the excessive growth of biological tissues that can

The associate editor coordinating the review of this manuscript and approving it for publication was Vishal Srivastava.

be divided into three main types: benign, premalignant, and malignant (cancer) ones [12]. Unlike normal tissue, malignant tumors contain cancer cells, which aggressively invade the surrounding tissues such as vessels and lymph nodes. The resulting metastases also alter the tissue morphology and microcirculation. Typically, histology is used as a golden standard for the determination of a tumor type in clinical diagnostics. However, the histologic examination of biopsy tissues is an invasive and time-consuming method that can lead to misdiagnosis due to a sampling error. Therefore, a noninvasive diagnostic method involving real-time imaging is more preferable for this purpose. Previous clinical studies and trials have demonstrated that lasers can be effectively used for treating brain, skin, and liver cancers [13]–[15].

Imaging-guided laser therapy approaches were able to significantly improve treatment accuracy and prevent additional damage to the normal tissue from the occurrence. These techniques included ultrasound imaging [16], magnetic resonance imaging [17], and fluorescence microscopy [18]. However, because the spot size of a treatment laser typically ranges from tens of micrometers to millimeters, the resolution of the imaging technique should be limited to the micrometer scale such as those of fluorescence microscopy and optical coherence tomography (OCT) [19], [20]. Among various optical imaging methods, OCT can achieve a micrometer-scale resolution with an imaging depth of 2−3 mm. Moreover, OCT is based on the backscattering of biological tissues and does not require using any exogenous contrast agents. Additionally, OCT possesses basic functional imaging abilities for the identification of tissue characteristics. In the case of OCT angiography (OCTA), various methods including speckle variance [21], [22], decorrelation [23], Doppler effect [24], and optical micro-angiography [25] have been developed. Considering the use of OCT as guidance for laser therapy, Boppart *et al.* first demonstrated that laser ablation could be dynamically monitored by high-resolution OCT [26]. Kaufmann *et al.* proposed to integrate OCT and selective retinal therapy with a pulsed laser for the real-time monitoring of treatment outcome in the case of retinal pigment epithelium [27]. Moreover, Katta *et al.* demonstrated an integrated system combining OCT and laser ablation for conducting a precise and bloodless tumor surgery [28]. In previous studies, pulsed lasers were used for ablation, which significantly increased the cost and size of the treatment system. Additionally, Beaudette *et al.* proposed to use a double-clad fiber coupler to integrate a two-dimensional OCT and a CW modulated Raman fiber laser centered at 1436 nm for tissue coagulation [29]. However, the proposed configuration was based on a Michelson interferometer, making dynamically adjusting the incident power on the sample to optimize the imaging sensitivity difficult. Moreover, only two-dimensional OCT imaging was utilized to identify the difference in the tissue morphology and the backscattered intensity along with the depth after laser coagulation, and thus it was difficult to investigate the photothermal effect in a three-dimensional perspective. To monitor the induced photothermal effect due to laser exposure, Lo *et al.* evaluated the complex difference variance from the OCT results [30]. A tunable fiber laser with a tuning range from 1860 nm to 1895 nm was implemented for laser thermal therapy. To examine the tissue coagulation induced by laser exposure, 10 consecutive B-scans were required for the CDV estimation and the *ex vivo* results of different biological tissue were demonstrated. Repeated scans might be a problem to be applied to *in vivo* experiments.

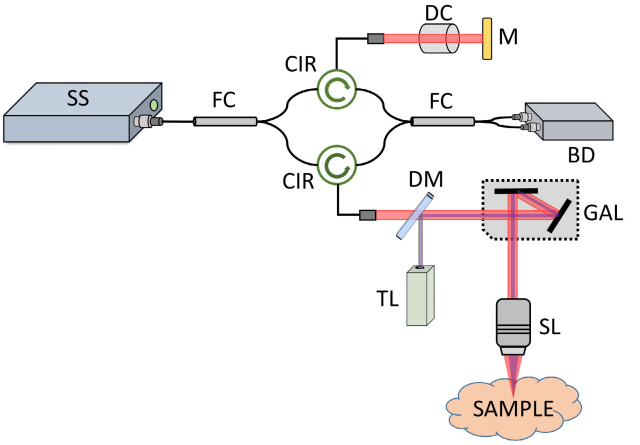

FIGURE 1. Schematic of the OCT-guided laser ablation system. SS: swept source, FC: fiber coupler, CIR: circulator, GAL: galvanometer, DM: dichroic mirror, SL: scanning lens, TL: treatment laser, DC: dispersion compensator, M: mirror.

As mentioned previously, high-power short-pulse lasers have become the most commonly used solution for laser therapy or ablation. However, high costs and bulky volumes of these instruments significantly limit their clinical applications. In this study, a CW laser diode was integrated with a swept source (SS)-OCT/OCTA system for the feasibility studies of laser ablation and tumor removal. OCT was used for the in vivo evaluation of induced photothermolysis and determination of the heating region. Additionally, the integrated system was implemented for the identification of the tumor region and evaluation of the treatment outcome. Moreover, the backscattering intensities of the ablated and non-ablated tissues were compared, and the vessel densities determined before and after laser ablation were quantitatively analyzed. Finally, the proposed method was applied to in vivo tumor removal.

II. EXPERIMENTAL SETUP

A. OCT-GUIDED LASER ABLATION SYSTEM

Figure 1 shows the schematic diagram of the developed OCT-guided laser ablation system. In this setup, a MEM-based swept source (HSL-20, Santec Corp., Komaki, Japan) was utilized; its center wavelength and tuning spectral range were 1310 and 110 nm, respectively. The sweep rate of the light source was 100 kHz, which corresponded to an A-scan rate of 100 kHz. The light source was connected to a fiber-based Mach-Zehnder interferometer, which split the light beam into the reference and sample arms. The interferometer was

composed of two fiber circulators and two fiber couplers with different coupling ratios. In the reference arm, a reflective mirror was fixed on a single-axis translational stage to adjust the optical path difference between the sample and reference arms. In the sample arm, a two-axis galvanometer (GVS002, Thorlabs, New Jersey, USA) was used for beam scanning. A dichroic mirror (DMLP735B, Thorlabs, New Jersey, USA) was installed before the galvanometer to combine the OCT and treatment laser beams. Finally, the two beams passed through the galvanometer and were focused on the sample by a scanning lens (LSM02, Thorlabs, New Jersey, USA). The utilized treatment laser contained a CW laser diode with a center wavelength of 450 nm. The maximum output power of the laser diode can reach up to 6 W. To study the feasibility of using a CW laser diode for laser treatment, the incident power focusing on the sample was only set to 4 W to avoid the extra damage and too rapid tissue reaction which may cause the difficulty in the observation of the induced changes with OCT/OCTA. The used laser diode is under multimode operation, and the beam diameter after the focusing lens in the sample arm was measured approximately 550 μm, corresponding to an energy fluence of 1.68×10^3 J/cm^2 incident on the sample. The laser diode costs ~US $80. Because the absorption coefficient of hemoglobin is higher at 450 nm, laser energy can be easily absorbed by red blood cells and converted into heat for tissue ablation [31]. In our experiment, the OCT frame rate was set to 100 frames/s, and each frame consisted of 1000 A-scans. Both the micromorphology and microvasculature of tissues were simultaneously determined by OCT imaging. During the OCTA analysis procedure, the same skin location was scanned twice, after which the speckle variance between two sequential images was calculated to obtain vascular information [32]. Each in three-dimensional (3D) OCTA data set consisted of $1000 \times 1000 \times 1024$ voxels ($X \times Y \times Z$). The measured axial and transverse resolutions of the OCT system were 7 and 10 μm, respectively.

B. EXPERIMENTAL ANIMALS

In this study, C57BL/6 wild-type mice with ages of 7–8 weeks were used. To investigate the feasibility of utilizing a 450-nm laser diode for tissue ablation, the normal mouse ear skin was exposed to its light beam and scanned with the OCT/OCTA system before and after laser exposure. Additionally, the OCT-guided laser therapy system was applied for *in vivo* tumor ablation. A dorsal skin window chamber implemented on the C57BL/6 mice was used to observe the tumor growth and outcome of laser ablation. A detailed procedure for the preparation of this chamber has been described in a previous study [33]. Briefly, the window chamber consisted of two complementary titanium frames with a circular observation area having an inner diameter of 11 mm. The observation area was made of a laterally positioned fold of dorsal skin sandwiched between the two frames. One side of the folded skin was removed and covered with a round glass piece fixed by a snap ring. Two microliters of phosphate-buffered saline solution containing 1×10^5 transgenic adenocarcinoma of

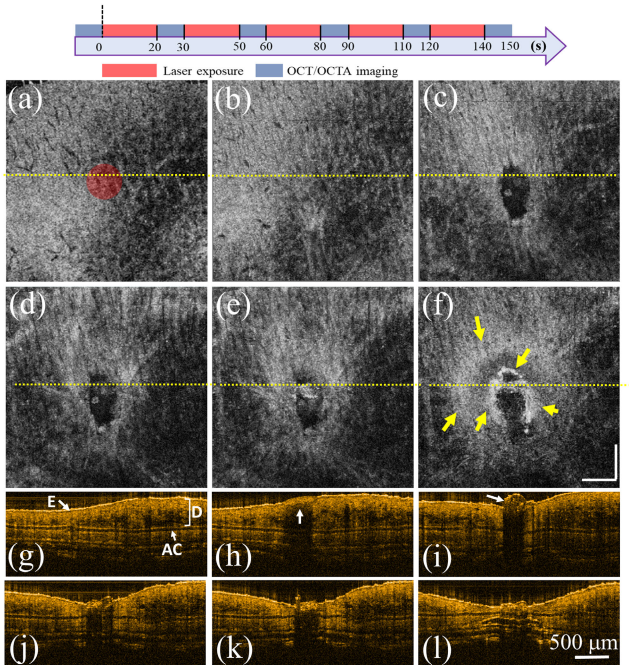

FIGURE 2. ***En-face*** **OCT images of the mouse ear skin obtained (a) before laser exposure and after the laser exposures at an average incident power of 4 W on the sample for (b) 20, (c) 40, (d) 60, (e) 80, and (f) 100 s. (g)–(l) Corresponding 2D OCT images of the mouse ear skin obtained for the closer locations indicated by the yellow-dash lines in panels (a)–(f). The scale bars in panels (f) and (l) denote the length of 500 μm. E: Epidermis, D: dermis, and AC: auricular cartilage.**

the mouse prostate (TRAMP) tumor cells were injected into the dermis at the center of the observation area. The growth of tumor cells was monitored by either a fluorescent microscope or OCT/OCTA at various time points. Because the inner diameter of the window chamber was 11 mm, it required four individual 3D scans to cover the entire window area, and the resulting images were combined into one 3D image. As the OCT beam was merged with the treatment laser beam on a common-path configuration as shown in Fig. 1, the treatment beam was guided to the center of the treated region using the obtained OCT/OCTA results by adjusting the driving voltages of the two-axis galvanometer before laser ablation. While only A-scans could be conducted in the center of the treated region during laser ablation, 3D OCT/OCTA imaging was performed before and after the laser ablation procedure. In this study, six normal mouse ears were involved and 11 mice with the dorsal skin tumor were used for the laser treatment.

III. RESULTS

To explore the feasibility of using the CW laser diode for tissue ablation, mouse ear skin was exposed to the laser beam with an average incident power of 4 W on the sample for different times followed by repeatedly scanning with OCT/OCTA. To examine the relationship between the induced photodamage and the exposure time, a selected skin area was scanned with OCT/OCTA before laser exposure,

after which it was exposed to the 450-nm laser beam for 20 seconds (s) and scanned with OCT/OCTA again. The same experimental procedure was repeated until the total exposure time of 100 s was achieved. Figure 2 shows the *en-face* OCT images extracted from the 3D images at a depth of 100 μm beneath the skin surface and the corresponding two-dimensional (2D) OCT results obtained for the locations indicated by the yellow-dash lines in Figs. 2(a)−(f). The latter represents the *en-face* images obtained before and after the laser exposures for 20, 40, 60, 80, and 100 s, respectively. The red circle in Fig. 2(a) denotes the incident area of the treatment laser. Note that the damage induced by the laser exposure for 40 s can be clearly identified (Fig. 2(c)) and that the backscattering intensity for the surrounding tissue of the ablated area gradually changed with the exposure time. After the total exposure for 100 s, the backscattering intensity significantly increased (see the yellow arrows in Fig. 2(f)) as compared with the results presented in Figs. 2(c)−(e). Such a variation in the backscattering intensity was caused by the thermal diffusion from the exposure area to the surrounding tissue that changed its composition. Additionally, Figs. 2(g)−(l) show the 2D images of Figs. 2(a)−(f) obtained from the indicated locations for better comparison. It is difficult to identify the changes in tissue architectures induced by laser exposure in Fig. 2(b), but the difference in the backscattering intensity can be clearly observed in Fig. 2(h) as indicated by the white arrow. As the exposure time increased, a blister was formed at a total exposure time of 40 s (see the white arrow in Fig. 2(i)). Afterward, this blister collapsed in Fig. 2(j), and the backscattering intensity in the surrounding area significantly increased, as shown in Fig. 2(l).

Moreover, it can be noted from Fig. 2 that laser exposure changed the backscattering properties of the tissue because photon energy significantly affected its composition and morphology. Therefore, further analysis of the backscattering intensity variation enables the detection of the damaged skin region. As shown in Fig. 3(a), firstly, the skin surface of each B-scan was detected according to the previously proposed method, and then, the skin surface of each B-scan was realigned to be flattened [34]. After that, the intensity distribution at the same depth along the transverse direction was obtained. Fig. 3(b) displays the distributions of the backscattering intensity along the transverse direction at a depth of 100 μm beneath the skin surface (i.e., within the epithelium region) obtained from Figs. 2(g)−(l) after the procedure outlined in Fig. 3(a).

Fig. 3(b) shows the variation of the OCT backscattering intensity along the transverse direction before and at the different time points after the laser exposure initiated (i.e., different exposure), which can be used for identifying the difference between the ablated and non-ablated tissues. After the surface flattening procedure, every eleven B-scans adjacent to the locations indicated by the yellow lines in Figs. 2(g)−(l) were selected for the estimation of the mean and standard deviation (STD) values of the intensity distribution along the transverse direction at a depth of 100 μm beneath the

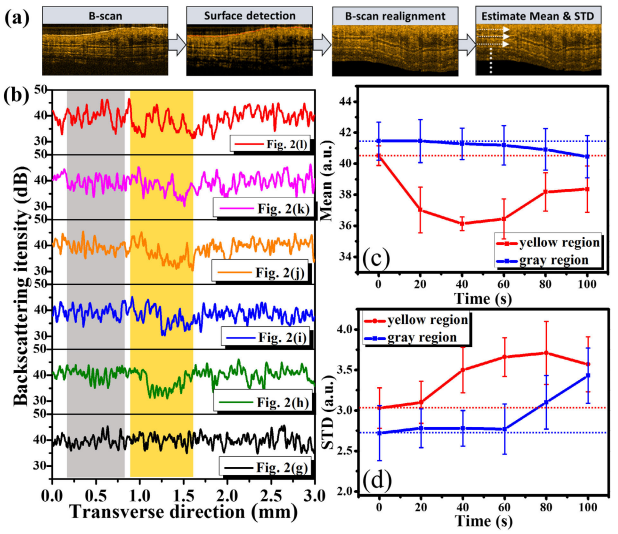

FIGURE 3. (a) Flowchart of the developed algorithm for estimating the intensity variation along with the skin depth. (b) Distributions of the backscattering intensity along the transverse direction obtained from Figs. 2(g)−(l) at a depth of 100 μm beneath the tissue surface after processing. (c)(d) Mean backscattering intensity and STD values of the gray and yellow regions estimated from Figs. 2(g)−(l) at the same skin depths.

skin surface (see Figs. 3(c) and (d)). Here, the yellow region, as shown in Fig. 3(b) covers a transverse distance of 1 mm including both the exposed and surrounding (non-exposed) areas. Additionally, a transverse distance of 1 mm was selected for the gray region, representing the non-exposed area. The laser exposure altered the tissue composition and morphology, leading to the variation in the mean backscattering intensity. The red curve in Fig. 3(c) plotted for the yellow region including both the exposed and surrounding regions significantly changed after laser exposure. Although the blue curve in Fig. 3(c) represents the results obtained for the gray region, the mean value for the blue curve gradually decreased after the total exposure for 60 s, which likely resulted from the thermal diffusion from the exposed region to the surrounding one. The data presented in Fig. 3(d) also shows that the STD of the backscattering intensity along the transverse direction increases after laser exposure, as shown by the red curve (the exposed region) in Fig. 3(d). As the exposure time increases, the STD values of the red curve continue to increase, and the STD values of the blue curve (the unexposed region) slightly change after 60 s, suggesting that the generated heat diffused into the unexposed region.

As previously mentioned, OCTA imaging can be simultaneously performed to identify the microvasculature of mouse skin. Figure 4 shows the maximum-intensity-projection OCTA images over a depth range of 1.5 mm, corresponding to the OCT results depicted in Fig. 2 that were obtained before and after the laser exposures for 20, 40, 60, 80, and 100 s. Figures 4(a)−(f) indicate that the vessels in the exposed area disappeared after the laser exposure for 20 s, while the black area gradually became larger with increasing exposure

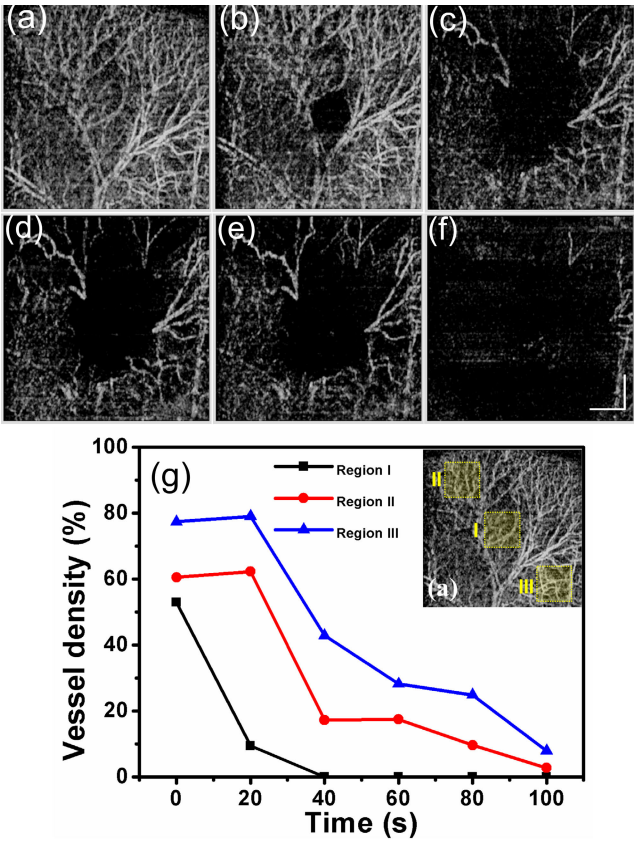

FIGURE 4. Maximum-intensity-projection OCTA images corresponding to the results depicted in Fig. 2, which were obtained (a) before laser exposure and after the laser exposures at an incident power of 4 W for (b) 20, (c) 40, (g) 60, (h) 80, and (i) 100 s. (g) Vessel densities estimated for the three areas indicated by the yellow squares in the inset at various exposure times. The scale bars represent the length of 500 μm.

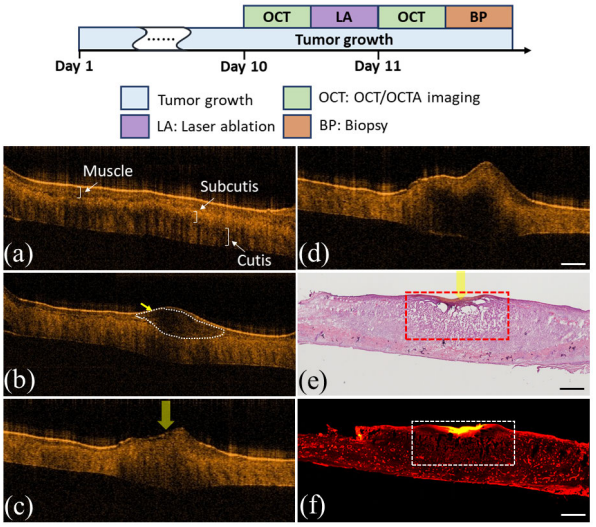

FIGURE 5. 2D OCT images of the mouse skin extracted at the close location from the 3D images obtained on (a) Day 1 after implantation, (b) Day 10 after implantation, (c) Day 10 after laser ablation, and (d) Day 11. (e) Histological data corresponding to the image displayed in panel (d). (f) Corresponding CD31 microscopic image. The white outline indicates the tumor region, and the scalar bar denotes the length of 500 μm.

time. Because the OCTA algorithm is based on measuring the time-dependent intensity variance at the same tissue location, the disappearance of vessels from the OCTA images indicates that either the blood flow over the irradiated region was stopped or the microvascular network was destructed. Moreover, the vessel densities in Figs. 4(a)−(f) were quantitatively analyzed according to the algorithm developed in a previous study [32]. Three individual areas denoted by the yellow squares in Fig. 4(a) were selected to estimate the vessel densities at various exposure times in the inset of Fig. 4(g) (Regions I, II, and III). The obtained results indicate that the vessel density in the central area (Region I) is reduced to zero after a 40-s exposure, while those in the upper and lower regions (Regions II and III) decreased to zero after 100 s of laser exposure, owing to the heat diffusion from the exposed area (Region I). These data also demonstrate that the estimated vessel density can be effectively used to identify the heating area, which is typically larger than the exposed area.

Figures 3 and 4 show that the tissues damaged by laser exposure can be distinguished from unexposed tissues by measuring the intensity variation along the transverse direction and vessel density. To further investigate the feasibility of using the integrated laser system for tumor removal, an experiment involving the tumorous animal model and dorsal skin window chamber was conducted. Tumor cells were implanted into the mouse skin, and OCT scanning was performed to monitor tumor growth and determine the outcome of the laser ablation procedure. Figures 5(a) and (b) display the 2D OCT images of the mouse skin extracted at a closer location from the 3D images obtained on Days 1 and 10 after the tumor cell implantation, respectively. In Fig. 5(a), different layer structures can be identified including the muscle layer, subcutis, and cutis. After subcutaneous implantation of tumor cells for 10 days, the tumor region can be identified from the OCT result as indicated by the white outline in Fig. 5(b). From Fig. 5(b), it can be found that the scattering intensity of the tumor tissue is significantly weaker than that of the normal tissue. Therefore, the tumor region can be identified according to the scattering property. In our experiments, the laser exposure was performed when the tumor size reached 1.5 mm in width which can be measured from the OCT results. According to the OCT results obtained on Day 10 as shown in Fig. 5(b), the targeted treatment region was identified, and the beam of the treatment laser was directed toward the tumor center by adjusting the tilting angles of the galvanometer. Subsequently, the tumor center was exposed to the 450-nm laser beam at a power of 4 W for 100 s. Figure 5(c) shows the OCT image obtained after laser ablation, and the scan in Fig. 5(d) was acquired 24 h after laser ablation. The yellow arrow in Fig. 5(c) denotes the exposure location. Here, the laser exposure changed the backscattering intensity of the exposed region as compared with that in the OCT images obtained before exposure. The same skin area was scanned

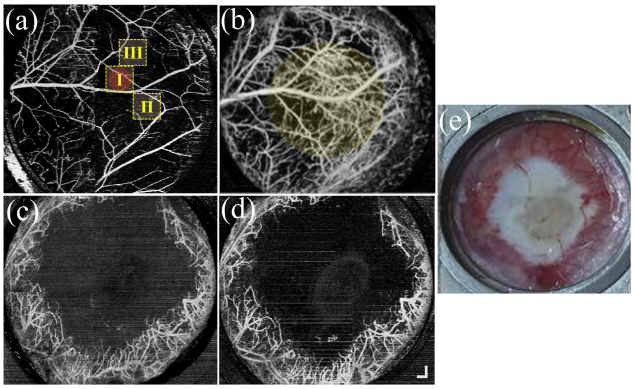

FIGURE 6. (a)–(d) OCTA scans corresponding to the images depicted in Figs. 5(a)–(d). (e) A photograph of the skin window chamber taken after laser exposure. The scale bars denote the length of 500 μm.

again 24 h later, as shown in Fig. 5(d). To validate the obtained OCT results, the mouse was sacrificed, and the skin locations specified in Figs. 5(a)–(d) were selected for biopsy.

The resulting histological image (Fig. 5(e)) can be used to locate the heating area; it also shows that the composition and morphology of the mouse skin have significantly changed. Because CD31 is a platelet endothelial cell adhesion molecule 1 (PECAM-1) which can be a vascular marker, CD31 microscopic results are used to validate the OCTA results in our experiments as shown in Fig. 5(f) [35]. In Fig. 5(f), the dark red spots represent the damaged vessels induced by laser exposure, and the bright red parts indicate the vessels without photodamage. Since the maximal absorption regime of hemoglobin ranges from 410 to 420 nm, the exposure time can be further reduced by using the laser diodes with either shorter wavelengths or higher output powers to render a higher absorption efficiency.

Apart from the OCT results, the corresponding OCTA data are presented in Fig. 6. Figure 6(a) shows the projection-view OCTA image of the mouse skin within the window chamber that was obtained on Day 1 after tumor cell implantation; the same skin area was scanned again on Day 10 after implantation, as shown in Fig. 6(b). The red circle in Fig. 6(a) (overlapped with yellow-dash box for region I) denotes the implantation area. The angiogenesis induced by tumor growth is indicated by the yellow circle in Fig. 6(b), and the 450-nm laser beam was incident on the center of the tumor region for ablation. After the laser exposure for 100 s, the vessels in the central region of the window chamber disappeared (Fig. 6(c)), suggesting that laser ablation destroyed the vessels and stopped the blood flow. Furthermore, Fig. 6(d) displays the OCTA results obtained 24 h after laser exposure, which also does not contain the disappeared vessels, illustrating that the ablation procedure can effectively damage the tissue and vessels. Finally, Fig. 6(e) shows the photograph of the window chamber taken before the histological examination. The white region in this figure denotes the ablated area, and the vessels can still be observed in the surrounding area without thermal damage. These results show that the

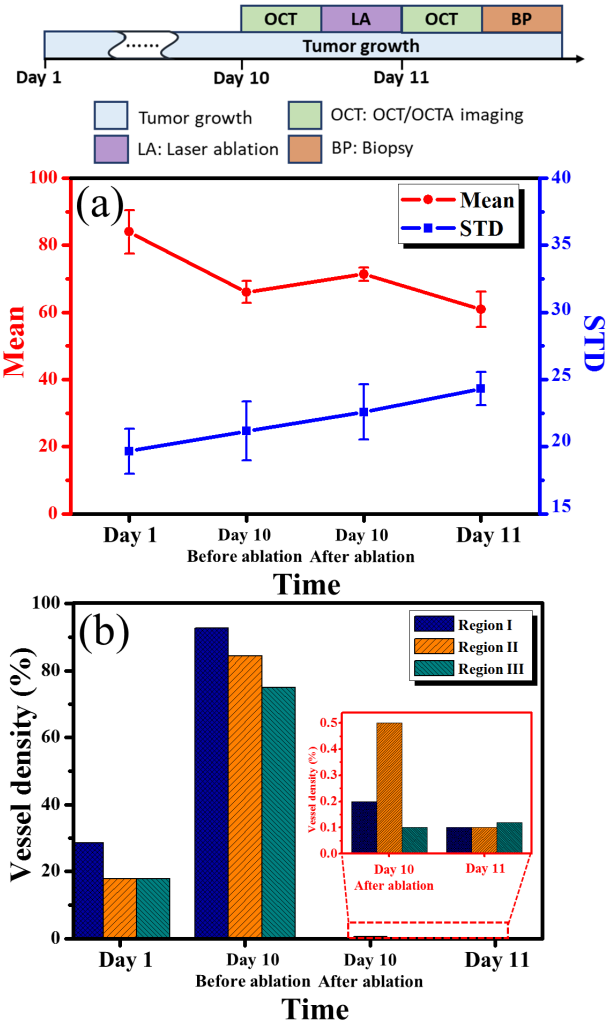

FIGURE 7. (a) Mean intensity and STD values estimated along the transverse direction on Day 1, Day 10 before ablation, Day 10 after ablation, and 24 h after ablation. (b) Vessel densities estimated on Day 1, Day 10 before ablation, Day 10 after ablation, and 24 h after ablation.

photodamage induced by the CW laser may be monitored by OCT/OCTA for tumor removal. Similar to the results presented in Figs. 3 and 4, the changes in the intensity distribution along the transverse direction and vessel density were evaluated as well. Every eleven B-scans adjacent to each B-scan in Figs. 5(a)–(d) were selected for the estimation of the mean and STD values of the intensity distribution along the transverse distance of 1 mm at a depth of 100 μm beneath the skin surface. Additionally, to identify the changes in the tumor region induced by laser ablation, the areas denoted by the yellow squares in Fig. 6(a) (Regions I, II, and III) were selected for evaluation.

Figure 7(a) displays the mean intensity (red curve) and STD (blue curve) values determined along the transverse direction at different time points, including Day 1, Day 10 before laser exposure, Day 10 after laser ablation, and 24 h later after laser ablation. For the red curve, the mean intensity

decreased during tumor growth and slightly increased after laser ablation. After 24 h, the mean value decreased and remained smaller than the intensity estimated on Day 1. For the blue curve, the STD value continuously increased with time, indicating that the tumor growth and laser ablation processes increased the intensity variation. These results are similar to the data presented in Fig. 3(c), suggesting that laser heating changed the backscattering intensity of the biological tissue. To analyze the changes in the vessel density, the three regions denoted by the yellow squares in Fig. 6(a) were selected. The inset of Fig. 7(b) displays the magnified data obtained immediately after laser exposure and 24 h later. They show that the vessel density increased because of the angiogenesis that occurred during tumor growth. However, the vessel density suddenly decreased after laser ablation, and no significant changes in its values were observed in 24 h, indicating that the tumor was successfully removed by the OCT-guided CW laser ablation procedure.

IV. DISCUSSION

Pulsed lasers have been widely used in clinical therapy, and the photodamage caused by their use can be easily controlled. However, the high cost and bulky size of these lasers significantly limit their clinical applications. Thus, in this work, we used a low-cost CW laser diode to examine the feasibility of tumor removal under the OCT/OCTA guidance. Using this procedure, a treatment region was identified, and the treatment outcome was effectively monitored. Moreover, the photodamaged area was determined by OCT/OCTA to prevent additional damage to the surrounding tissues caused by the laser beam.

From Fig. 5, the abnormal tissue region can be distinguished by identifying the difference in the backscattered property and the morphological change between the normal and abnormal tissues. Additionally, tumor growth causes angiogenesis, thereby increasing the vessel density in the cancerous region. Consequently, the vessel density in a specific area obtained on Day 1 and Day 10 were compared to recognize the normal and cancerous tissues. Thus, OCT/OCTA was used for the identification of normal and abnormal tissues before laser ablation, and the treatment laser beam was guided according to the obtained OCT/OCTA images. In order to control the incident location of the laser beam on the sample surface, a dichroic mirror was inserted before the galvanometer in the current design of the sample arm that combined OCT with the treatment beams. In the resulting setup, the incident angle of the treatment beam on the sample surface could be easily adjusted by the galvanometer according to the region of interest determined from the OCT/OCTA results. During laser exposure, both beams are fixed at the same location. Meanwhile, only OCT M-mode scans can be performed to observe the dynamics of laser ablation at the exposure location. However, B-mode and C-mode scans may not be conducted during laser exposure, making the dynamic observation of the photothermal effect on the surrounding tissue very difficult. Alternatively, the dichroic mirror can be inserted after the galvanometer; in this case, the combined beams may be focused through the lens in the sample arm, and only the OCT beam is driven by the galvanometer, while the treatment beam is fixed in the middle of the lens without scanning. To change the skin location for laser exposure, additional translational stages must be installed to focus the treatment beam at the region of interest. However, the latter approach is difficult to implement in an *in vivo* study. Therefore, in this work, the dichroic mirror was inserted before the galvanometer.

As shown in Figs. 2 and 5, laser ablation alters the composition and morphology of biological tissues, thus changing their optical properties and microcirculation. At the beginning of laser exposure, laser beam irradiation results in the formation of blisters that later collapse. In previous studies, it was demonstrated that the tissue temperature was proportional to the exposure time and that the scattering coefficient increased with temperature [36], [37]. As shown in Fig. 2(l), the scattering intensity increases in the exposed region and surrounding tissues, which is consistent with the results of earlier works. The same phenomenon is seen in Figs. 5(c) and (d). Although the observed changes in the tissue morphology and optical properties are different in these two figures, it is difficult to determine the photothermal effect for the surrounding tissue from the OCT results. Meanwhile, the CW laser diode with a center wavelength of 450 nm was used for tissue ablation, and the absorption coefficient of hemoglobin at 450 nm is higher than the values obtained at longer wavelengths. Therefore, the photon energy can be efficiently absorbed by hemoglobin and then transformed into heat. Thus, OCTA can be helpful in studying tissue microcirculation, which is strongly affected by the angiogenesis occurring during tumor growth. Moreover, OCTA results can serve as guidance for positioning the laser ablation beam because the absorption efficiency is optimal when the treatment laser is incident on a vessel-rich region. Additionally, it is difficult to evaluate the photodamage of the surrounding tissue caused by OCT; however, its degree can be determined by OCTA.

For the treatment with CW lasers, laser energy can be absorbed by biological tissue and red blood cells, and then, transferred to the thermal effect. Although the usage of a 450-nm laser diode may penetrate a shallower depth than the lasers with longer wavelengths, the heat can be transferred to the surrounding and even deeper tissue for treatment purposes. Additionally, our histological results in Figs. 5(e) and 5(f) also indicate that the deeper tissue layer can be coagulated when the 450-nm laser diode was used. Therefore, the integration of the 450-nm laser diode with the OCT/OCTA system is feasible for tumor therapy in a depth range of 1 mm. Compared to other commercial CW lasers, the used 450-nm laser diode in the visible spectral range is commercially available, and the small size is easy to be integrated with an OCT system for *in vivo* applications. To further avoid the disruption from the damaged surface and to treat the deeper tissue, a needle-type OCT/OCTA-guided laser therapy system can be implemented [38]. In the previous

experiments, the tumor tissue can be ablated for an exposure time of 100 s with an exposure power of 4 W on it. However, the exposure time can be further improved by increasing the exposure power. The utilization of CW laser diodes with higher absorption efficiencies for hemoglobin or water is also beneficial to optimize the exposure period [39]. Additionally, the exposure time can be further reduced with the needle-type OCT/OCTA-guided laser surgery system.

V. CONCLUSION

In conclusion, the low-cost CW laser diode with a center wavelength of 450 nm was utilized for laser ablation and integrated with the SS-OCT system having a center wavelength of 1310 nm. Using this setup, both OCT and OCTA images were simultaneously obtained. To investigate the feasibility of laser ablation with the 450-nm laser diode, mouse skin was exposed to its beam, and the exposed region was scanned with OCT/OCTA. The resulting changes in the skin morphology and optical properties were determined from the OCT images, and a method for investigating the alternation of the scattering intensity was proposed to differentiate between the non-ablated and ablated tissues. Moreover, OCTA was used for observing tissue microcirculation and evaluating the photothermal effect quantitatively from the estimated vessel density. Finally, the developed OCT/OCTA-guided laser ablation system was utilized for tumor removal. From the obtained results, it can be concluded that a tumor may be effectively removed by the 450-nm laser diode and that the photodamaged area can be monitored and controlled under the guidance of OCT/OCTA. Hence, the developed OCT/OCTA-guided laser therapy system is advantageous in terms of cost and treatment efficiency.

REFERENCES

[1] H. J. Song, H.-J. Seo, Y. Lee, and S. K. Kim, "Effectiveness of high-intensity laser therapy in the treatment of musculoskeletal disorders: A systematic review and meta-analysis of randomized controlled trials," *Medicine*, vol. 97, no. 51, Dec. 2018, Art. no. e13126.

[2] H.-W. Choi, J. Lee, S. Lee, J. Choi, K. Lee, B.-K. Kim, and G.-J. Kim, "Effects of high intensity laser therapy on pain and function of patients with chronic back pain," *J. Phys. Therapy Sci.*, vol. 29, no. 6, pp. 1079–1081, 2017.

[3] M. Nikfarjam and C. Christophi, "Interstitial laser thermotherapy for liver tumours," *Brit. J. Surgery*, vol. 90, no. 9, pp. 1033–1047, 2003.

[4] Y. M. Paulus, A. Jain, R. F. Gariano, B. V. Stanzel, M. Marmor, M. S. Blumenkranz, and D. Palanker, "Healing of retinal photocoagulation lesions," *Investigative Opthalmol. Vis. Sci.*, vol. 49, no. 12, pp. 5540–5545, Dec. 2008.

[5] D. M. Brown, W. C. Ou, T. P. Wong, R. Y. Kim, D. E. Croft, and C. C. Wykoff, "Targeted retinal photocoagulation for diabetic macular edema with peripheral retinal nonperfusion," *Ophthalmology*, vol. 125, no. 5, pp. 683–690, May 2018.

[6] A. Giorgio, L. Tarantino, G. de Stefano, N. Farella, O. Catalano, B. Cusati, L. Del Viscovo, A. Alaia, and E. Caturelli, "Interstitial laser photocoagulation under ultrasound guidance of liver tumors: Results in 104 treated patients," *Eur. J. Ultrasound*, vol. 11, no. 3, pp. 181–188, Jun. 2000.

[7] T. Omi and K. Numano, "The role of the CO_2 laser and fractional CO_2 laser in dermatology," *Laser Therapy*, vol. 23, no. 1, pp. 49–60, 2014.

[8] V. Vachiramon, W. Panmanee, T. Techapichetvanich, and K. Chanprapaph, "Comparison of Q-switched nd: YAG laser and fractional carbon dioxide laser for the treatment of solar lentigines in Asians," *Lasers Surgery Med.*, vol. 48, no. 4, pp. 354–359, Jan. 2016.

[9] T. Knebel, A. Streek, and H. Exner, "Comparison of high rate laser ablation and resulting structures using continuous and pulsed single mode fiber lasers," *Phys. Procedia*, vol. 56, pp. 19–28, Jan. 2014.

[10] T. Ma, Y. Chai, H. Zhu, H. Chen, Y. Wang, Q. Li, L. Pang, R. Wu, Y. Lv, and D. Dong, "Effects of different 980-nm diode laser parameters in hepatectomy," *Lasers Surgery Med.*, vol. 51, no. 8, pp. 720–726, May 2019.

[11] J. T. Hashmi, Y. Y. Huang, S. K. Sharma, D. B. Kurup, L. De Taboada, J. D. Carroll, and M. R. Hamblin, "Effect of pulsing in low-level light therapy," *Laser Surg. Med. J*, vol. 42, no. 6, pp. 450–466, Jul. 2010.

[12] P. Hahnfeldt, D. Panigrahy, J. Folkman, and L. Hlatky, "Tumor development under angiogenic signaling: A dynamical theory of tumor growth, treatment response, and postvascular dormancy," *Cancer Res.*, vol. 59, no. 19, pp. 4770–4775, Oct. 1999.

[13] S. Missios, K. Bekelis, and G. H. Barnett, "Renaissance of laser interstitial thermal ablation," *Neurosurgical Focus*, vol. 38, no. 3, p. E13, Mar. 2015.

[14] P. Avci, A. Gupta, M. Sadasivam, D. Vecchio, Z. Pam, N. Pam, and M. R. Hamblin, "Low-level laser (light) therapy (LLLT) in skin: Stimulating, healing, restoring," *Semin. Cutan. Med. Surg.*, vol. 32, no. 1, p. 41, Mar. 2013.

[15] S. Sartori, F. Di Vece, F. Ermili, and P. Tombesi, "Laser ablation of liver tumors: An ancillary technique, or an alternative to radiofrequency and microwave?" *World J. Radiol.*, vol. 9, no. 3, p. 91, 2017.

[16] G. He, C. Zheng, M.-A. Yu, and H. Zhang, "Comparison of ultrasound-guided endovenous laser ablation and radiofrequency for the varicose veins treatment: An updated meta-analysis," *Int. J. Surgery*, vol. 39, pp. 267–275, Mar. 2017.

[17] R. Medvid, A. Ruiz, R. J. Komotar, J. R. Jagid, M. E. Ivan, R. M. Quencer, and M. B. Desai, "Current applications of MRI-guided laser interstitial thermal therapy in the treatment of brain neoplasms and epilepsy: A radiologic and neurosurgical overview," *Amer. J. Neuroradiology*, vol. 36, no. 11, pp. 1998–2006, Jun. 2015.

[18] A. L. Lazarides, M. J. Whitley, D. B. Strasfeld, D. M. Cardona, J. M. Ferrer, J. L. Mueller, H. L. Fu, S. B. DeWitt, B. E. Brigman, N. Ramanujam, D. G. Kirsch, and W. C. Eward, "A fluorescence-guided laser ablation system for removal of residual cancer in a mouse model of soft tissue sarcoma," *Theranostics*, vol. 6, no. 2, pp. 155–166, 2016.

[19] J. Odenthal, P. Friedl, and R. P. Takes, "Compatibility of CO_2 laser surgery and fluorescence detection in head and neck cancer cells," *Head Neck*, vol. 41, no. 5, pp. 1253–1259, Dec. 2018.

[20] N. Katta, A. B. McElroy, A. D. Estrada, and T. E. Milner, "Optical coherence tomography image-guided smart laser knife for surgery," *Lasers Surgery Med.*, vol. 50, no. 3, pp. 202–212, Aug. 2017.

[21] M. S. Mahmud, D. W. Cadotte, B. Vuong, C. Sun, T. W. H. Luk, A. Mariampillai, and V. X. D. Yang, "Review of speckle and phase variance optical coherence tomography to visualize microvascular networks," *J. Biomed. Opt.*, vol. 18, no. 5, Apr. 2013, Art. no. 050901.

[22] A. Mariampillai, B. A. Standish, E. H. Moriyama, M. Khurana, N. R. Munce, M. K. K. Leung, J. Jiang, A. Cable, B. C. Wilson, I. A. Vitkin, and V. X. D. Yang, "Speckle variance detection of microvasculature using swept-source optical coherence tomography," *Opt. Lett.*, vol. 33, no. 13, pp. 1530–1532, Jun. 2008.

[23] Y. Jia, O. Tan, J. Tokayer, B. Potsaid, Y. Wang, J. J. Liu, M. F. Kraus, H. Subhash, J. G. Fujimoto, J. Hornegger, and D. Huang, "Split-spectrum amplitude-decorrelation angiography with optical coherence tomography," *Opt. Express*, vol. 20, no. 4, pp. 4710–4725, Feb. 2012.

[24] R. A. Leitgeb, R. M. Werkmeister, C. Blatter, and L. Schmetterer, "Doppler optical coherence tomography," *Prog. Retin. Eye Res.*, vol. 41, pp. 26–43, Jul. 2014.

[25] L. An, J. Qin, and R. K. Wang, "Ultrahigh sensitive optical microangiography for *in vivo* imaging of microcirculations within human skin tissue beds," *Opt. Express*, vol. 18, no. 8, pp. 8220–8228, Apr. 2010.

[26] S. A. Boppart, J. Herrmann, C. Pitris, D. L. Stamper, M. E. Brezinski, and J. G. Fujimoto, "High-resolution optical coherence tomography-guided laser ablation of surgical tissue," *J. Surgical Res.*, vol. 82, no. 2, pp. 275–284, Apr. 1999.

[27] D. Kaufmann, C. Burri, P. Arnold, V. M. Koch, C. Meier, B. Považay, and J. Justiz, "Selective retina therapy enhanced with optical coherence tomography for dosimetry control and monitoring: A proof of concept study," *Biomed. Opt. Express*, vol. 9, no. 7, pp. 3320–3334, Jun. 2018.

[28] N. Katta, A. D. Estrada, A. B. McElroy, A. Gruslova, M. Oglesby, A. G. Cabe, M. D. Feldman, R. D. Fleming, A. J. Brenner, and T. E. Milner, "Laser brain cancer surgery in a xenograft model guided by optical coherence tomography," *Theranostics*, vol. 9, no. 12, pp. 3555–3564, 2019.

[29] K. Beaudette, H. W. Baac, W.-J. Madore, M. Villiger, N. Godbout, B. E. Bouma, and C. Boudoux, "Laser tissue coagulation and concurrent optical coherence tomography through a double-clad fiber coupler," *Biomed. Opt. Express*, vol. 6, no. 4, pp. 1293–1303, Mar. 2015.

[30] W. C. Y. Lo, N. Uribe-Patarroyo, A. S. Nam, M. Villiger, B. J. Vakoc, and B. E. Bouma, "Laser thermal therapy monitoring using complex differential variance in optical coherence tomography," *J. Biophotonics*, vol. 10, no. 1, pp. 84–91, Sep. 2016.

[31] W. G. Zijlstra and A. Buursma, "Spectrophotometry of hemoglobin: Absorption spectra of bovine oxyhemoglobin, deoxyhemoglobin, carboxyhemoglobin, and methemoglobin," *Comparative Biochem. Physiol. B, Biochem. Mol. Biol.*, vol. 118, no. 4, pp. 743–749, Dec. 1997.

[32] W.-J. Chen, Y.-Y. Chang, S.-C. Shen, Y.-L. Tzeng, H.-C. Lee, C.-H. Yang, and M.-T. Tsai, "*in vivo* detection of UV-induced acute skin effects using optical coherence tomography," *Biomed. Opt. Express*, vol. 9, no. 9, pp. 4235–4245, Aug. 2018.

[33] M. W. Laschke, B. Vollmar, and M. D. Menger, "The dorsal skinfold chamber: Window into the dynamic interaction of biomaterials with their surrounding host tissue," *Eur. Cells Mater.*, vol. 22, pp. 147–167, Sep. 2011.

[34] C.-H. Yang, M.-T. Tsai, S.-C. Shen, C. Y. Ng, and S.-M. Jung, "Feasibility of ablative fractional laser-assisted drug delivery with optical coherence tomography," *Biomed. Opt. Express*, vol. 5, no. 11, pp. 3949–3959, Oct. 2014.

[35] V. Vanchinathan, N. Mizramani, R. Kantipudi, E. J. Schwartz, and U. N. Sundram, "The vascular marker CD31 also highlights histiocytes and histiocyte-like cells within cutaneous tumors," *Amer. J. Clin. Pathol.*, vol. 143, no. 2, pp. 177–185, Feb. 2015.

[36] R. C. Niemeier, S. Etoz, D. A. Gil, M. C. Skala, C. L. Brace, and J. D. Rogers, "Quantifying optical properties with visible and near-infrared optical coherence tomography to visualize esophageal microwave ablation zones," *Biomed. Opt. Express*, vol. 9, no. 4, pp. 1648–1663, Mar. 2018.

[37] M. O. D. Santos, A. Latrive, P. A. A. De Castro, W. De Rossi, T. M. T. Zorn, R. E. Samad, A. Z. Freitas, C. L. Cesar, N. D. V. Junior, and D. M. Zezell, "Multimodal evaluation of ultra-short laser pulses treatment for skin burn injuries," *Biomed. Opt. Express*, vol. 8, no. 3, pp. 1575–1588, Feb. 2017.

[38] C.-P. Liang, J. Wierwille, T. Moreira, G. Schwartzbauer, M. S. Jafri, C.-M. Tang, and Y. Chen, "A forward-imaging needle-type OCT probe for image guided stereotactic procedures," *Opt. Express*, vol. 19, no. 27, pp. 26283–26294, Dec. 2011.

[39] Y.-J. Lee, Z.-P. Yang, F.-Y. Lo, J.-J. Siao, Z.-H. Xie, Y.-L. Chuang, T.-Y. Lin, and J.-K. Sheu, "Slanted n-ZnO/p-GaN nanorod arrays light-emitting diodes grown by oblique-angle deposition," *APL Mater.*, vol. 2, no. 5, May 2014, Art. no. 056101.